



Hydrogen-controlled structural reconstruction of palladium-bismuth oxide cluster to single atom alloy for low-temperature CO oxidation

Bing Nan^{a,d,*}, Lulu Li^{b,1}, Yunan Li^d, Lingling Guo^{a,d}, Meng Du^{a,d}, Zhengwu Liu^d, Xin Tao^d, Chen Tian^d, Zhenye Liang^d, Yanxing Zhang^{c,**}, Chao Ma^e, Lu Shen^f, Rui Si^{d,**}, Lina Li^{a,d,*}

^a Shanghai Synchrotron Radiation Facility, Zhangjiang Laboratory, Shanghai Advanced Research Institute, Shanghai 200120, China

^b State Key Laboratory for Modification of Chemical Fibers and Polymer Materials, College of Environmental Science and Engineering, Donghua University, Shanghai 201620, China

^c School of Physics, Henan Normal University, Xinxiang 453007, China

^d Shanghai Institute of Applied Physics, Chinese Academy of Sciences, Shanghai 201204, China

^e Center for High Resolution Electron Microscopy, College of Materials Science and Engineering, Hunan University, Changsha 410082, China

^f Division of China, TILON Group Technology Limited, Shanghai 200090, China

ARTICLE INFO

Keywords:

Metal oxide clusters
Single atom alloy
Structure evolution
CO oxidation

ABSTRACT

Palladium (Pd) has been widely regarded as a high-performance catalyst for various oxidative reactions, however, the actual structure of active site remains controversial due to structural evolution under operation conditions. Herein, we prepared a series of bismuth (Bi)-doped silica-supported Pd catalysts and found a hydrogen-controlled structural reconstruction mechanism of palladium-bismuth oxide cluster to single atom alloy to efficiently catalyze low-temperature CO oxidation. The formation of $\text{Pd}_x\text{Bi}_y\text{O}_z$ clusters with unique Pd–O–Bi coordination structure could enhance the sinter-resistance ability of Pd species. This structural evolution of active site is clearly uncovered by in-situ XAFS results, in which metallic Bi–Pd shell gradually generates as the increase of reduction temperature without any metallic Bi–Bi bond. More importantly, PdBi_1 single atom alloy exhibits a good CO oxidation activity with a CO_2 production rate of $413 \mu\text{mol}_{\text{CO}_2} \cdot \text{g}_{\text{Pd}}^{-1} \cdot \text{s}^{-1}$ at 100°C and excellent catalytic stability. Density function calculation (DFT) results indicate that there are geometric and electronic effects between Bi and Pd atoms, which favor total linear-CO adsorption, activate CO and O_2 molecules, and reduce the barrier for the formation of OO-CO intermediates in PdBi_1 single atom alloy.

1. Introduction

The construction of active site is an efficient and common method to acquire excellent catalytic performance in heterogeneous catalytic reactions, including single atom site, active interfaces, alloy and so on [1–6]. When the size of material is at nanometer or sub-nanometer scale, the active sites frequently undergo significantly structural reconstruction and compositional changes in supported catalysts, due to complex pretreatment, reaction and post-treatment conditions, such as reducing atmosphere, pressure, and temperature [7–10]. Accordingly, the structure evolution of active species always results in the variation of catalytic performance and catalytic stability, via offering abundant oxygen vacancies [11], active surface oxygen [12], unique adsorption behavior

[13] and coordination environment [14]. Somorjai and co-workers reported that PtSn intermixed metallic components under reducing conditions reversibly separated into isolated domains of Pt and oxidic Sn under reaction conditions, which greatly improved CO oxidation activity by supplying oxygen species [9]. Tao et al. also found $\text{Rh}_{0.5}\text{Pd}_{0.5}$ nanoparticles underwent dramatic and reversible changes in composition and chemical state in response to oxidizing or reducing conditions due to the flexibility and tunability of bimetallic nanoparticle [10]. In addition, these constructions of active site can only be observed under certain conditions and ex situ characterization often leads to diverse and unreliable conclusions. Thus, it is significant to construct highly efficient and stable active species by definitive structural evolution and provide a clear and reliable description of “structure-activity” relationship in CO

* Corresponding authors at: Shanghai Synchrotron Radiation Facility, Zhangjiang Laboratory, Shanghai Advanced Research Institute, Shanghai 200120, China.

** Corresponding authors.

E-mail addresses: nanb@sari.ac.cn (B. Nan), zhangyanxing@htu.edu.cn (Y. Zhang), sirui@mail.sysu.edu.cn (R. Si), lilina@sinap.ac.cn (L. Li).

¹ Bing Nan and Lulu Li contributed equally to this manuscript.

oxidation via comprehensive ex/in situ microscopy and spectroscopy techniques.

The CO oxidation to carbon dioxide ($\text{CO} + 1/2 \text{O}_2 = \text{CO}_2$) is one of the most extensively researched reactions in heterogeneous catalysis, as a crucial step to resolve automobile exhaust containing CO, NO and hydrocarbons in industrial application [15–18]. The wide temperature range of exhausts demands high-performance catalysts at low-temperature with good catalysis stability. Palladium, as a representative noble metal, exhibits a promising catalytic activity in CO elimination and utilization, due to variation of oxidation state and distinctive electronic structure [19]. However, the serious deactivation problem of Pd catalysts restricts its further application in the practical industry. Recently, many main group elements, such as Sn [9], Na [4], and Bi [20,21], were as promoters in Pt- and Co-based catalysts to enhance the activity and stability of various oxidation reactions (CO oxidation and selective oxidation of glycerol). Among them, Bi species is a good dopant to promote CO oxidation by providing sufficient oxygen vacancies [20], preventing the overoxidation of noble metal [22], and regulating adsorption behavior [23]. Thus, it is a feasible strategy to add bismuth element to supported Pd catalysts to improve low-temperature CO oxidation activity.

Moreover, single atom alloys (SAAs) have received extensive research in multifarious reactions, such as selective hydrogenations [24], C–O coupling [25], and CO oxidation [26], and these SAAs materials are comprised of single atoms of a catalytically active metal (Pd, Pt, Rh, Ni) alloyed into the surface of a less reactive host metal (Cu, Ag, Au, Bi) [27]. The SAAs sample could provide many unique properties including improved activity/selectivity and catalytic stability vs the monometallic counterparts [24], oxygen dissociation ability [28] and resistance to CO poisoning [29]. In addition, according to previous reports [30,31], PdBi SAAs catalysts with Bi at atomical dispersion exhibited an excellent electrochemical CO_2 reduction and ethanol oxidation activity, which could decrease energy barrier of rate-determining step. It indicates that PdBi SAAs catalyst possess absolutely different physicochemical properties with pure palladium catalyst in reductive and oxidation reactions. To the best of our knowledge, almost no research is about PdBi SAAs to catalyze CO oxidation, and the precise local coordination and electronic structure of PdBi SAAs are still unclear.

Herein, we have prepared a series of silica-supported palladium-bismuth catalysts via an incipient wetness impregnation for CO oxidation. In fresh Bi-promoted samples, the formation of $\text{Pd}_x\text{Bi}_y\text{O}_z$ binary oxide clusters (<2 nm) could greatly enhance the sinter-resistance ability of Pd species via strong interaction between palladium and bismuth (Pd–O–Bi structure). An obvious structural evolution regulated by hydrogen reduction occurred in Bi-promoted samples, in which $\text{Pd}_x\text{Bi}_y\text{O}_z$ oxide clusters transformed to PdBi_1 single atom alloy with bismuth at atomical level. This single atom alloy catalyst exhibits excellent performance in CO oxidation with a reaction rate at $413 \mu\text{mol}_{\text{CO}_2} \cdot \text{g}_{\text{Pd}}^{-1} \cdot \text{s}^{-1}$ at 100 °C, which was about ten times that of pure palladium-silica catalyst. Combining a kinetic study and theoretical calculations, a low barrier for forming OO-CO intermediates and rapid O removal play a key role in high-performance in CO oxidation.

2. Experimental section

2.1. Catalyst preparation

All of the chemicals applied to our experiments are of analytical grade and were used without further purification or modification. Bismuth (III) nitrate pentahydrate ($\text{Bi}(\text{NO}_3)_3 \cdot 5 \text{H}_2\text{O}$, AR) and Palladium (II) nitrate dihydrate ($\text{Pd}(\text{NO}_3)_2 \cdot 2 \text{H}_2\text{O}$, CP) were purchased from Sinopharm Chemical Reagent Co., Ltd. Silicon dioxide (SiO_2 , $S_{\text{BET}} = 688 \text{ m}^2/\text{g}$) was obtained from Evonik Specialty Chemicals (Shanghai) Co., Ltd.

SiO_2 was calcinated at 400 °C for 4 h (ramping rate: 2 °C/min) to remove surface water before catalysts preparation. The deposition of

palladium and bismuth onto SiO_2 support was carried out by a co-incident wetness impregnation (IMP). Firstly, a solution of $\text{Bi}(\text{NO}_3)_3$ (50–124 mg respective) and $\text{Pd}(\text{NO}_3)_2$ (25 mg) in 1.0 mol/L HNO_3 (3 mL) was added dropwise onto SiO_2 powder (1 g) under manually stirring. The powders were standing in ambient conditions for 2 h and then dried in still air at 80 °C for 12 h, followed by air-calcination at 550 °C for 4 h (ramping rate: 2 °C/min). The Bi and Pd contents were controlled on demand during preparation process of catalysts, and the data of these catalysts is as follows:

- 1 Pd- SiO_2 (1 wt% Pd, 0 wt% Bi),
- 1Pd2Bi- SiO_2 (1 wt% Pd, 2 wt% Bi),
- 1Pd5Bi- SiO_2 (1 wt% Pd, 5 wt% Bi),
- 1Pd1Bi- SiO_2 (1 wt% Pd, 5 wt% Bi),
- 2Bi- SiO_2 (2 wt% Bi).

2.2. Catalytic activity tests

CO oxidation activities for Pd/PdBi- SiO_2 samples were evaluated in a fix bed reactor using 30 mg of sieved (20–40 mesh) powders in a gas mixture of 1 vol% CO, 20 vol% O_2 and 79 vol% N_2 (from Jinan Deyang Corporation, 99.997% purity) at a flow rate of 66.7 mL/min giving a gas hourly space velocity (GHSV) of $\sim 134,000 \text{ mL} \cdot \text{g}_{\text{cat}}^{-1} \cdot \text{h}^{-1}$. The catalysts were pretreated in 5% H_2/He (50 mL/min) at 180 °C for 30 min before reaction. After catalysts cooled down to room temperature under a flow of pure N_2 gas, reactant gases were passed through reactor. The outlet gas compositions of CO and CO_2 were monitored online by nondispersive IR spectroscopy (Gasboard 3500, Wuhan Sifang Company, China). The related stability tests were done in the same conditions at the constant reaction temperature of 150 °C for 40 h with a GHSV of $\sim 200,000 \text{ mL} \cdot \text{g}_{\text{cat}}^{-1} \cdot \text{h}^{-1}$. CO conversion was defined as $\text{CO}_{\text{reaction}} / \text{CO}_{\text{input}} \times 100\%$. Rate measurements were made in the separate catalytic tests rather than the “light-off” mode, i. e. the same gas composition, but at specific space velocities to ensure operation in kinetic regime (< 20% conversion of CO).

2.3. Materials characterization

Powder X-ray diffraction (XRD) patterns were recorded on a Bruker D8 Advance diffractometer (40 kV, 40 mA) with a scanning rate of 4° min^{-1} , using $\text{Cu K}\alpha_1$ radiation ($\lambda = 1.5406 \text{ \AA}$). The diffraction patterns were collected from 20° to 80° with a step of 0.02° . The 2θ angles were calibrated with a μm -scale alumina disc. The powder sample after grinding was placed inside a quartz sample holder for each test.

Nitrogen adsorption-desorption measurements were performed on an ASAP2020-HD88 analyzer (Micromeritics Co. Ltd.) at 77 K. The measured powders were degassed at 250 °C under vacuum ($< 100 \mu\text{mHg}$) for over 4 h. The BET specific surface areas (S_{BET}) were calculated from data in relative pressure range between 0.05 and 0.20 and pore diameter (D_p) distribution was calculated from the adsorption branch of isotherms, based on BJH method.

TEM and high-resolution TEM (HRTEM) experiments were carried out on a FEI Tecnai G [2] F20 microscope operating at 200 kV. All tested samples were suspended in ethanol, and then a drop of this dispersed suspension was placed on an ultra-thin (3–5 nm in thickness) carbon film-coated Cu grid. The as-formed sample grid was dried naturally under ambient conditions before being loaded into TEM sample holder. Furthermore, the aberration-corrected high-angle annular dark-field scanning transmission electron microscopy (HAADF-STEM) and related EDS mapping images were carried out on a JEOL ARM200F microscope equipped with a probe-forming spherical-aberration corrector.

The *ex-situ* and in situ X-ray absorption fine structure (XAFS) spectra at Pd K ($E_0 = 24350.0 \text{ eV}$) and Bi L_3 ($E_0 = 13419.0 \text{ eV}$) edge were performed at BL14W1 and 11B beamline respectively of Shanghai Synchrotron Radiation Facility (SSRF) operated at 3.5 GeV under “top-up” mode with a constant current of 220 mA. XAFS data were recorded

under fluorescence mode with a Lytle detector and the energy was calibrated accordingly to absorption edge of pure Pd and Bi foils. For in situ XAFS experiments, the powder sample (~ 25 mg) was pressed into a tablet (o.d. = 1.2 cm) and placed into a ceramic sample holder of in situ flow cell. All catalysts were in situ reduced in flow cell at different temperatures (100–180 °C) with 5 vol% H_2/N_2 for 0.5 h to detect the formation of PdBi_1 single atom alloy. The ramping rate was 5 °C/min under temperature programming, and the temperature was monitored with a 0.5 mm chromel–alumel thermocouple that was placed inside cell near sample. Athena and Artemis codes were used to extract data and fit profiles. For X-ray absorption near edge structure (XANES) part, experimental absorption coefficients as a function of energies $\mu(E)$ were processed by background subtraction and normalization procedures. Based on the normalized XANES profiles, the molar fraction of $\text{Pd}^{2+}/\text{Pd}^0$, and $\text{Bi}^{3+}/\text{Bi}^0$ can be determined by linear combination fit with the help of various references (Pd foil for Pd^0 and PdO for Pd^{2+} ; Bi foil for Bi^0 and Bi_2O_3 for Bi^{3+}). For extended X-ray absorption fine structure (EXAFS) part, fourier transformed (FT) data in R space were analyzed by applying PdO and metallic Pd model for Pd–O and Pd–Pd contributions. The passive electron factors, S_0^2 , were determined by fitting the experimental data on Pd foil and fixing the coordination number (CN) of Pd–Pd to be 12, and then fixed for further analysis of the measured samples. The parameters describing the electronic properties (e.g., correction to the photoelectron energy origin, E_0) and local structure environment including CN, bond distance (R), and Debye-Waller factor around the absorbing atoms were allowed to vary during the fit process.

The spin-polarized *ab initio* calculations are based on the DFT-D computations, as implemented in Dmol3 code embedded in Materials Studio [32]. The PBE functional [33] within generalized gradient approximation [34] (GGA) was utilized to describe the exchange-correlation interactions. The density functional theory (DFT) Semi-core Pseudopotentials [35] (DSPP) were employed to replace the core electrons for reducing the computational cost and the double numerical plus polarization (DNP) basis sets were chosen. During the structural geometry optimization, the convergence criteria were set as 10^{-7} Ha for energy, 0.001 Ha/Å for the force, and 0.005 Å for displacement. The electronic self-consistent field tolerance was set to 10^{-7} Ha for the electronic optimization. The global orbital cutoff of 4.7 Å and a smearing value of 0.005 Ha were specified for the orbit occupation to speed up convergence.

The temperature-programmed reduction by hydrogen (H_2 –TPR) and carbon monoxide (CO –TPR) was performed in an AutoChem II 2920 instrument (America) equipped with a thermal conductivity detector (TCD) and mass spectrometer (Tilon GRP Technology Limited LC-D200M). The fresh catalysts (40–60 mesh, 100 mg) were pretreated in pure O_2 at 300 °C for 30 min and cooled to room temperature in the same atmosphere. The reduction process was carried out in a mixture of 5 vol% H_2/Ar (30 mL/min) from room-temperature to 750 °C (5 °C/min) for H_2 –TPR. For CO –TPR, 150 mg samples (20–40 mesh) were pretreated under different conditions for 30 min or after CO oxidation, then the reduction process was carried out in 5 vol% CO/He (20 mL/min) from room-temperature to 500 °C (5 °C/min).

3. Results and discussion

3.1. The formation of $\text{Pd}_x\text{Bi}_y\text{O}_z$ oxide clusters

According to our previous study, the doping of bismuth in silica-supported platinum catalysts could significantly enhance the thermostability of platinum species via forming uniform $\text{Pt}_x\text{Bi}_y\text{O}_z$ oxide clusters [36]. Nowadays, we further introduced bismuth as a dopant into silica-supported palladium via co-incipient wetness impregnation method and deeply researched the doping effect of bismuth species. Table S1 summarizes main textural properties of fresh Pd/PdBi-SiO₂ samples, in which pure palladium and palladium-bismuth samples possess identical loading (0.8 wt%) of palladium element. The bulk

concentrations of bismuth element for 1Pd2Bi-SiO₂, 1Pd5Bi-SiO₂ are 2.6 and 5.8 wt% respectively, well consistent with target value. It indicates that the doping of Bi has no influence on the deposition of Pd on silica support. Meanwhile, Bi-free and Bi-doped samples have similar textural properties, such as S_{BET} values and the type of adsorption-desorption isotherms (Table S1 and Fig. S1).

Under the above conditions, we found that the doping of Bi species could also significantly enhance the anti-sintering property of palladium element. X-ray diffraction (XRD) results of Pd/PdBi-SiO₂ samples in Fig. 1a showed a great difference between Bi-free and Bi-doped samples. Only a wide peak around 22° (JCPDS card no.: 29–0085) appears in all fresh PdBi/Bi-SiO₂ samples without any Pd/PdO/Bi/Bi₂O₃ diffraction peaks even under a “slow-scan” mode (Fig. S2), which indicated Pd and Bi species were small-size amorphous clusters on SiO₂ support after air calcination. However, a broad diffraction peak at 33.9° attributed to {101} lattice plane of PdO (bct, JCPDS card no.: 43–1024) was observed in 1 Pd-SiO₂, revealing the formation of crystalline PdO particles due to poor interaction between silica and palladium. For comparison, Park and co-workers only prepared Pd@SiO₂ core/shell samples with an average size of ~ 4 nm for PdO particles even encapsulation in silica shell [37]. In addition, no obvious Bi/Bi₂O₃ peaks were observed in 2Bi-SiO₂, which demonstrated that Bi species can keep itself in small size very well.

Furthermore, we employed TEM and HRTEM to determine cluster size and element distribution of palladium and bismuth species in Pd/PdBi-SiO₂ samples under a microdomain view. Fig. S3 and S4 display that the average size of palladium oxide species (3.0 ± 0.7 nm) of 1 Pd-SiO₂ was bigger than that (2.3 ± 0.7 , 2.1 ± 0.5 nm for 1Pd2Bi-SiO₂ and 1Pd5Bi-SiO₂ respective) of Bi-doped samples. The corresponding aberration-corrected HAADF-STEM images in Fig. 1b,c and S5 also confirmed the existence of large PdO particles (~ 5 nm) with obvious lattice fringe (0.26 nm) for {101} crystal plane, well consistent with the broad diffraction peak of PdO in XRD results (Fig. 1a). Only amorphous clusters (~ 2.0 nm) were observed in 1Pd2Bi-SiO₂ (Fig. 1d-f) without any lattice fringe of metallic Pd or PdO phases. The related aberration-corrected STEM-EDS elemental mapping images of 1Pd2Bi-SiO₂ determined that Pd and Bi elements were distributed in the same area and uniformly on the surface of SiO₂ (Fig. 1g), which demonstrated that bismuth was preferentially deposited near/on palladium species rather than SiO₂ support. Recently, Shan and coworkers also reported that Bi species could distribute uniformly on the surface of Pt nanowires [38].

3.2. The local coordination structure of $\text{Pd}_x\text{Bi}_y\text{O}_z$ clusters

We further employed X-ray adsorption fine structure to detect the precise coordination structure of bismuth and palladium. The XANES profiles at Pd K edge in Fig. 2a and Table S2 displayed that Pd species in all samples were mainly in Pd (II) state ($\delta = 1.9$, 1.8 and 1.8 for 1 Pd-SiO₂, 1 Pd2Bi-SiO₂ and 1Pd5Bi-SiO₂ respective) according to the linear combination fitting results in Fig. S6. However, a dramatical difference in extend X-ray adsorption fine structure (EXAFS) about distance (R) and coordination number (CN) was detected for Bi-free and Bi-doped samples. For 1 Pd-SiO₂, there was a typical coordination structure of PdO phase, with a strong Pd–O ($R \approx 2.04$ Å with CN ≈ 4.2) and Pd–O–Pd shell ($R \approx 3.12$ Å, CN ≈ 5.0) from PdO particles [39]. The CN value of Pd–O (~ 5.0) shell for 1 Pd2Bi-SiO₂ is slightly higher than that of 1 Pd-SiO₂, because the doping of Bi^{3+} species introduces more oxygen around palladium atoms. In addition, the CN of Pd–O–Pd (~ 1.2) shell for 1Pd2Bi-SiO₂ was much lower than that (~ 5.0) of 1 Pd-SiO₂, due to the generation of a new coordination structure (Pd–O–Bi shell) in Fig. 2b. The Pd–O–Bi shell at ~ 3.37 Å was distinctly different with the conventional Pd–O–Pd shell at ~ 3.12 Å (Fig. 3b). In addition, because of the formation of Pd–O–Bi structure, the distance of Pd–O–Pd shell (~ 3.07 Å) in Bi-doped samples was slightly shorter than that (~ 3.12 Å) of pure palladium sample. It indicated that the formation of Pd–O–Bi shell compressed the distance of Pd–O–Pd shell due to different ionic

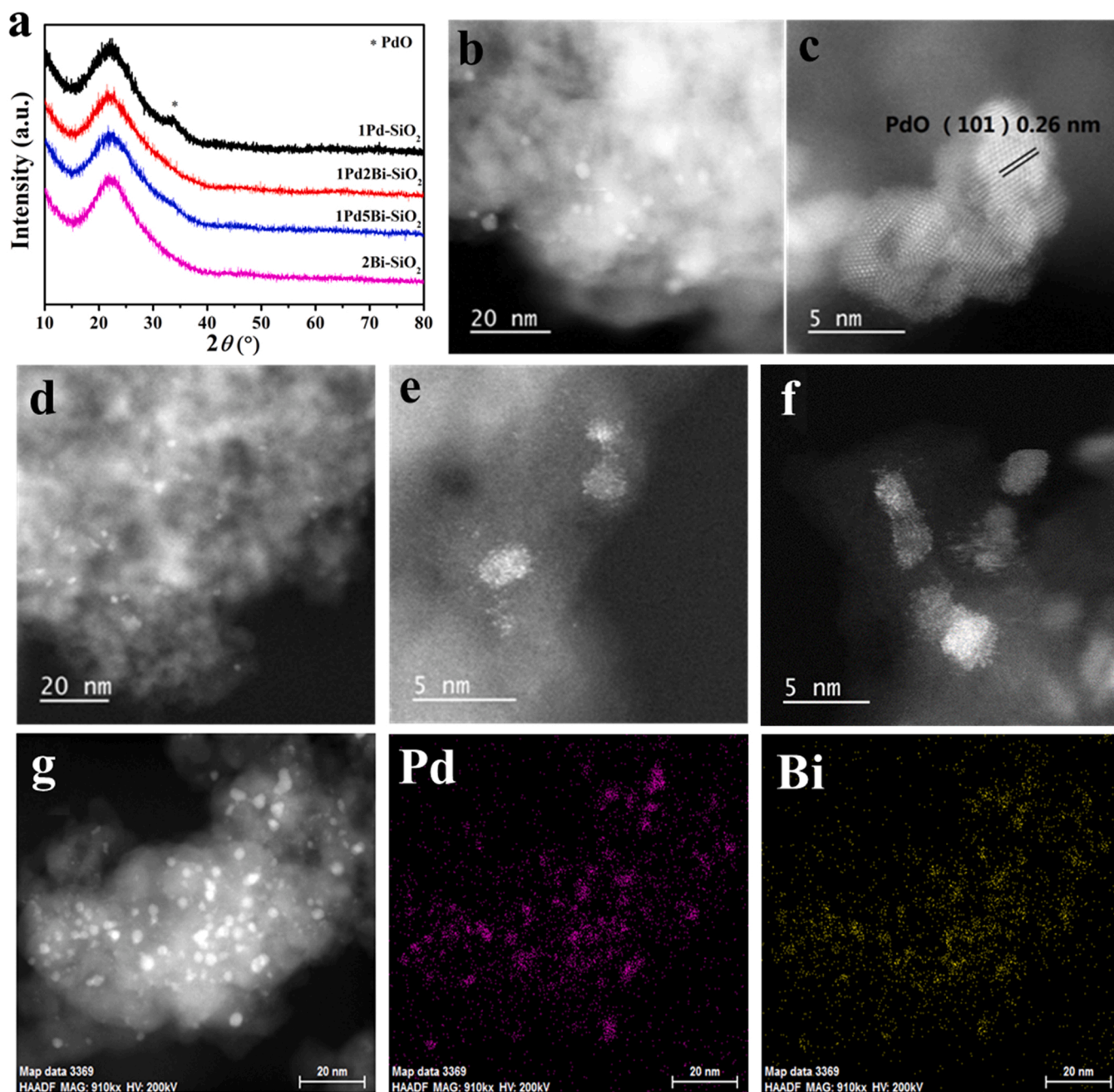


Fig. 1. (a) XRD patterns, (b-f) Aberration-corrected HAADF-STEM images of fresh Pd/PdBi-SiO₂ samples: (b-c) 1 Pd-SiO₂; (d-f) 1 Pd2Bi-SiO₂; and the corresponding EDS elemental mapping images of fresh (g) 1Pd2Bi-SiO₂.

radius for Bi³⁺ (1.03 Å) and Pd²⁺ (0.86 Å). Furthermore, the sum (~4.3) of coordination number of Pd–O–Pd and Pd–O–Bi shells in 1Pd2Bi-SiO₂ was almost equal to that (~5.0) over Pd–O–Pd shell on pure palladium sample in Table S2. Thus, we can conclude that bismuth atoms entered the interior of PdO_x clusters via forming Pd–O–Bi structure rather than anchoring on the surface of palladium oxide clusters, which was totally different from PdO cluster and particle. For 1Pd5Bi-SiO₂, there is a similar Pd–O–Bi structure with coordination number about 2.5 at ~3.37 Å in Fig. 2b and Table S2. It was supposed that the coordinated structure of Pd–O–Bi shell would not change dramatically with the increase of Bi species content.

Meanwhile, we also carried out XAFS experiments at Bi L₃ –edge to detect oxidation state and local coordination structure of bismuth species. As shown in Fig. 2c and Table S3, Bi species in Bi-doped samples was totally in Bi³⁺ state without any Bi⁰ phase, which excluded the

formation of PdBi alloy in fresh samples. For 1Pd2Bi-SiO₂, only a strong Bi–O shell ($R \approx 2.14$ Å, $CN \approx 2.3$) was determined, indicating bismuth species were at atomic level. However, when the loading of Bi species reaching ~5 wt%, an additional Bi–O–Bi ($R \approx 3.90$ Å, $CN \approx 1.3$) from BiO_x clusters was detected in 1 Pd5Bi-SiO₂, which also confirmed that excessive bismuth species tend to form isolated BiO_x clusters[40].

In addition, the H₂ –TPR experiment results also gave clear evidence about the generation of Pd–O–Bi interaction in Fig. 2e. There was a reduction peak at 62 °C in 1 Pd-SiO₂ in Fig. 2e due to the reduction of PdO_x clusters and a shoulder peak from the reduction of huge PdO particles in 1 Pd-SiO₂[41]. However, for 1Pd2Bi-SiO₂ and 1Pd5Bi-SiO₂, the first reduction peak obviously shifted to 144 and 206 °C respectively, demonstrating the formation of strong interaction between palladium and bismuth species (Pd–O–Bi structure), agreeing with EXAFS fitting results (Fig. 2b and Table S2). In addition, the DFT results

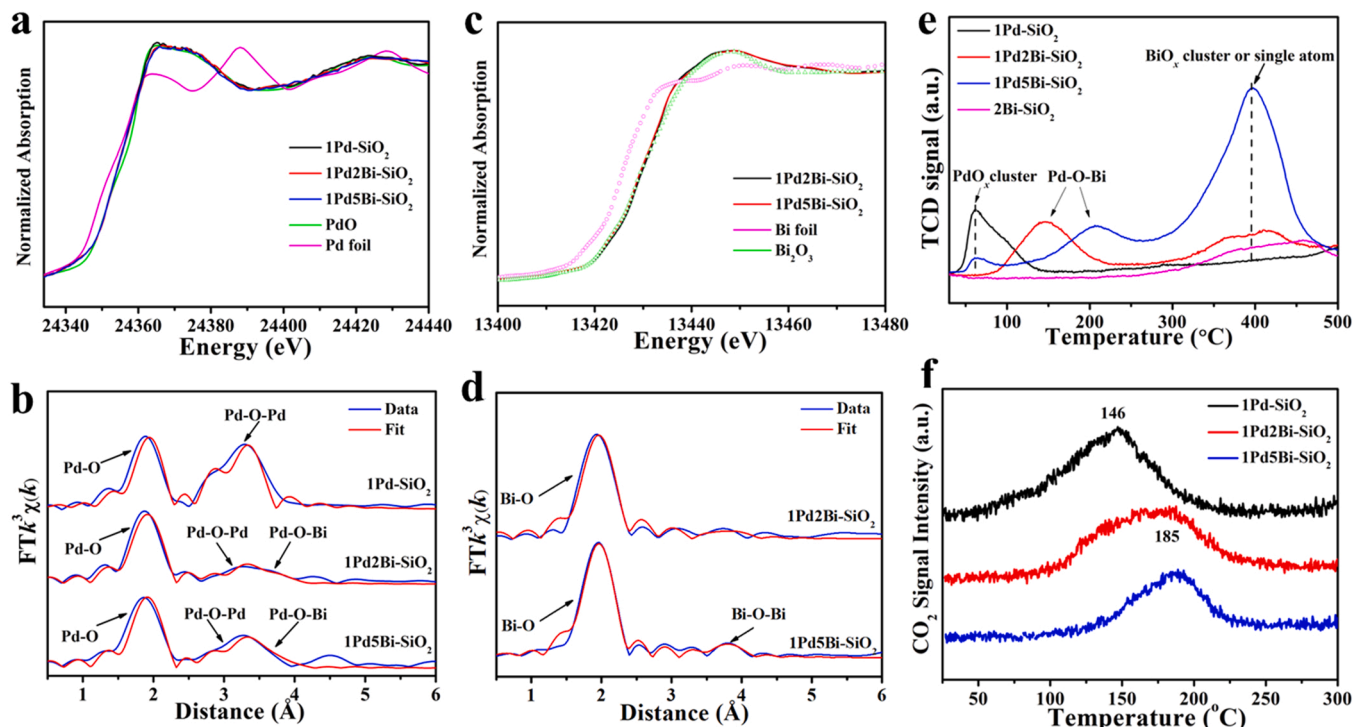


Fig. 2. Pd K-edge (a,b) and Bi L₃-edge (c,d) of XANES profiles (a, c) and EXAFS fitting results in R space (b, d) for fresh Pd/PdBi-SiO₂ samples; H₂ –TPR (e) and CO–TPR (f) experiments of fresh Pd/PdBi-SiO₂.

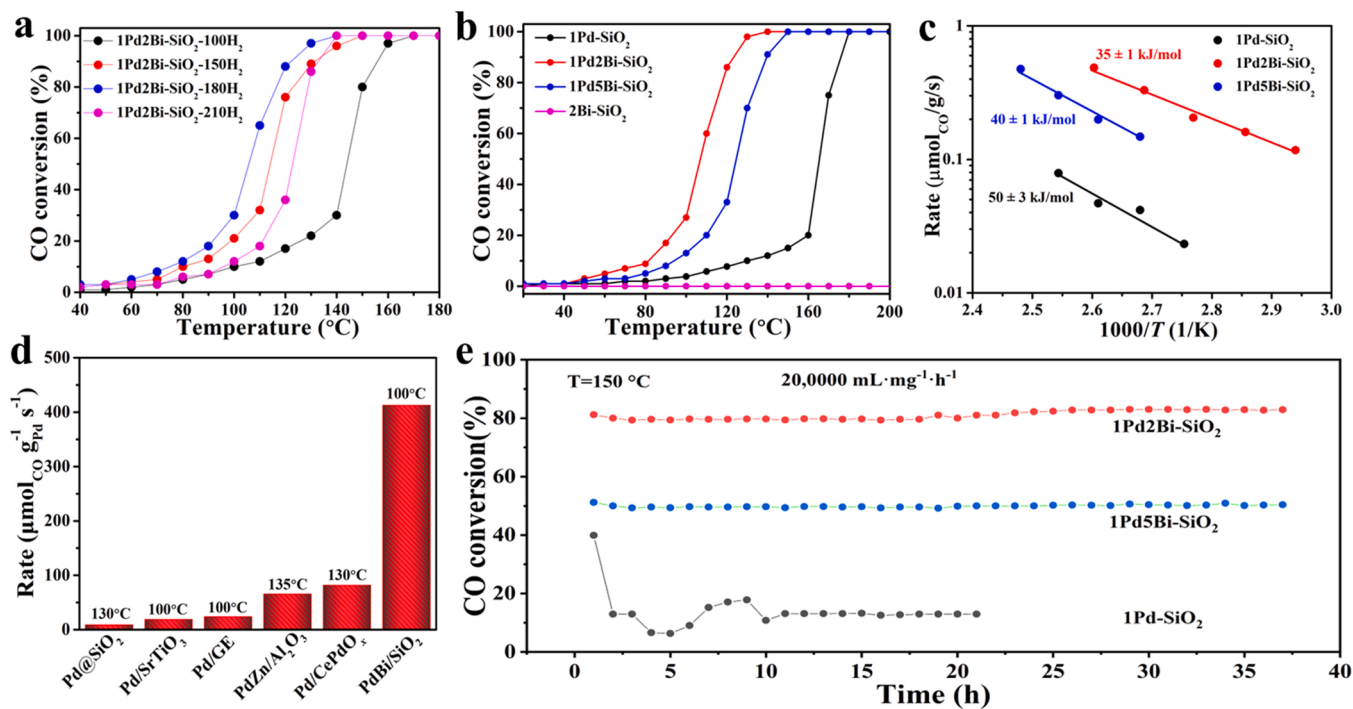


Fig. 3. (a) The effect of H₂-pretreatment at different temperature before CO oxidation experiment for 1Pd2Bi-SiO₂; (b) The “light-off” experiments over Pd/PdBi-SiO₂ samples, Catalysis condition: 1% CO/ 20% O₂/ 79% N₂, 134,000 mL g_{cat}⁻¹ h⁻¹; (c) Arrhenius plots for the oxidation of carbon monoxide; (d) The comparison of reaction rate over different catalysts for CO oxidation and (e) Stability tests for Pd/PdBi-SiO₂ samples.

also indicated the formation of Pd–O–Bi interaction increased cohesive energy about 0.43 eV, meaning better thermal stability of Pd_xO_yBi_z clusters (Fig. S7). Accordingly, CO–TPR results also confirmed that the formation of Pd–O–Bi structure in 1Pd2Bi-SiO₂ to some extent provided more surface oxygen (Fig. 2f). Besides, a small reduction peak of

isolated PdO_x cluster at ~60 °C was also observed in 1Pd5Bi-SiO₂, indicating that excessive doping of bismuth was detrimental to form interaction between Pd and Bi elements. There is a strong reduction peak at ~395 °C for 1Pd5Bi-SiO₂, which was attributed to the reduction of isolated BiO_x cluster or single atoms²¹. Therefore, we can make a clear

conclusion that the formation of unique $\text{Pd}_x\text{Bi}_y\text{O}_z$ clusters could enhance thermo-stability of palladium species.

3.3. Effects of reconstruction over active site in CO oxidation

The oxidation of carbon monoxide reaction ($2\text{CO} + \text{O}_2 = 2\text{CO}_2$) was used to evaluate the doping of bismuth species. Regrettably, Bi-doped palladium catalyst with higher dispersion of palladium exhibited worse CO oxidation activity in Fig. S8a, may due to improper active site [42]. Therefore, we tried to regulate active site structure via hydrogen reduction. A significant enhancement occurred in CO oxidation activity with hydrogen pretreatment at different temperatures for 1Pd2Bi-SiO₂ in Fig. 3a. The temperature of complete CO conversion dropped from 170 °C to 120 °C with hydrogen reduction temperature increasing from 100 °C to 180 °C. However, for 1 Pd-SiO₂, only a slight improvement in CO oxidation activity was observed after hydrogen reduction in Fig. S8b. Thus, it is highly possible to occur an active structure transformation during hydrogen reduction, rather than reduction of palladium species. Based on catalytic performance in Fig. 3b, there was a dramatical promotion to palladium-bismuth catalysts. 1Pd2Bi-SiO₂ showed the best CO oxidation activity by achieving 100% CO conversion at 130 °C under high gas hourly space velocity of $\sim 134,000 \text{ mL} \cdot \text{g}_{\text{cat}}^{-1} \cdot \text{h}^{-1}$. In contrast, 1 Pd-SiO₂ only achieve complete CO conversion at 180 °C. Recently, Du et al. achieved a 100% carbon monoxide conversion at 120 °C under a relatively low velocity ($\sim 80,000 \text{ mL} \cdot \text{g}^{-1} \cdot \text{h}^{-1}$) and with a reducible support (1.4 at% Pd/CeO₂ nanorod catalyst)¹⁹. Therefore, our palladium-bismuth catalysts exhibited good catalytic performance. The catalytic activity of PdBi-SiO₂ catalysts reached a maximum with bismuth loading of $\sim 2 \text{ wt\%}$, due to excessive Bi species hindering CO adsorption. 2Bi-SiO₂ exhibited no CO oxidation activity blew 200 °C, indicating bismuth species was just as a dopant to modify palladium species (Fig. 3b).

We collected kinetic data and calculated apparent activation energy (E_a) of all Pd/PdBi-SiO₂ samples to compare the inherent catalytic activity (Table S4). As shown in Fig. 3c and Table S5, 1Pd2Bi-SiO₂ exhibited lower value of E_a ($\sim 35 \text{ kJ/mol}$) closing to CeO₂ supported Pd catalysts ($\sim 40 \text{ kJ/mol}$) [43] and much lower than E_a value ($\sim 50 \text{ kJ/mol}$) of 1 Pd-SiO₂ and other inter supported palladium catalysts. Recently, Soni and co-workers reported similar E_a value of 73 kJ/mol for 2.8 wt% Pd-SBA-15 in CO oxidation [44]. It further demonstrated the formation of new active site or different reaction pathway after structure regulation via hydrogen reduction. Meanwhile, the reaction rate normalized by catalyst weight (r_w) of 1 Pd2Bi-SiO₂ ($r_w = 3.3 \mu\text{mol}_{\text{CO}} \cdot \text{g}_{\text{cat}}^{-1} \cdot \text{s}^{-1}$ at 100 °C) was about 8 times higher than that ($r_w = 0.4 \mu\text{mol}_{\text{CO}} \cdot \text{g}_{\text{cat}}^{-1} \cdot \text{s}^{-1}$ at 100 °C) of 1 Pd-SiO₂ (Table S5). Overmuch Bi dopant could result in slight declination of r_w value, may due to bismuth

coating palladium.

Furthermore, the reaction rate normalized by palladium weight (r_{Pd}) was compared with other reported Pd-based catalysts in Fig. 3d and Table 1. The r_{Pd} value of our 1Pd2Bi-SiO₂ ($413 \mu\text{mol}_{\text{CO}} \cdot \text{g}_{\text{Pd}}^{-1} \cdot \text{s}^{-1}$) was far higher than that ($9\text{--}88 \mu\text{mol}_{\text{CO}} \cdot \text{g}_{\text{Pd}}^{-1} \cdot \text{s}^{-1}$) of other monometallic and bimetallic palladium catalysts. It indicated that our palladium-bismuth catalysts possessed good catalytic performance. In addition, the Bi-doped palladium catalysts also presented remarkable catalytic stability, in which no obvious deactivation occurred at 150 °C with an ultrahigh space velocity at $200,000 \text{ mL} \cdot \text{g}_{\text{cat}}^{-1} \cdot \text{h}^{-1}$ for $\sim 40 \text{ h}$. However, there is an obvious deactivation in about two hours for pure palladium catalyst, due to surface oxidation or aggregation of palladium species.

3.4. The formation of PdBi₁ single atom alloy

According to catalytic performance and kinetic data, there was an obvious reconstruction of active site after hydrogen reduction in Bi-promoted samples compared with fresh catalysts. Thus, it is crucial to explore the true active site. As shown in Fig. 4a, the XRD profiles of all used Pd/PdBi-SiO₂ samples showed a tiny metallic Pd diffraction peak at 40.1° (fcc, JCPDS card no.: 46-1043), due to forming small size Pd⁰ particles after CO oxidation. For used 1 Pd5Bi-SiO₂, additional two small diffraction peaks at 27.9° and 46.4° were simultaneously observed, which could be attributed to Bi₂O₃ phase (monoclinic, JCPDS card no.: 41-1449), because of slight aggregation of excessive BiO_x clusters into crystalline Bi₂O₃ particles.

Based on TEM and HRTEM images in Fig. S9, after CO oxidation, there was an obvious aggregation of palladium species about $4.0 \pm 0.7 \text{ nm}$ (Fig. S4b) in 1 Pd-SiO₂ due to poor interaction between silica support and metallic palladium species. Moreover, the related aberration-corrected HAADF-STEM images in Fig. 4b,c and S10 also confirmed the existence of metallic Pd particles with an obvious lattice distance of 0.23 nm for (111) crystal plane. For 1Pd2Bi-SiO₂, most of palladium species was maintained in clusters (Fig. 4d,e). Interestingly, some brighter spots on the surface of metallic palladium clusters were observed in 1Pd2Bi-SiO₂, which may be bismuth single atoms according to Z value of palladium (46) and bismuth (83) in Fig. 4f. In addition, the corresponding aberration-corrected STEM-EDS elemental mapping result of 1Pd2Bi-SiO₂ in Fig. 4g depicted that palladium and bismuth elements were still distributed at the same area and uniformly and Bi element was dispersed at single atom level.

XAFS technique was employed to determine electronic and local coordination structure of active site in Bi-free and Bi-doped catalysts. The XANES profiles in Fig. 6a revealed that Pd species in used samples was mainly metallic Pd phase (average oxidation state of 0.5 and 0.3 for 1 Pd-SiO₂ and 1Pd2Bi-SiO₂ respective) due to hydrogen reduction,

Table 1

Comparison of catalytic activity for 1Pd2Bi-SiO₂ with other reported active Pd based catalysts.

Catalyst	Tem. (°C)	r_w ($\mu\text{mol}_{\text{CO}} \cdot \text{g}_{\text{cat}}^{-1} \cdot \text{s}^{-1}$)	r_{Pd} ($\mu\text{mol}_{\text{CO}} \cdot \text{g}_{\text{Pd}}^{-1} \cdot \text{s}^{-1}$)	E_a (kJ/mol)	Ref.
1Pd2Bi-SiO ₂ (0.8 wt% Pd)	100	3.3	413	35	This work
2.5 wt% Pd/La-Al ₂ O ₃	140	0.6	24	62	[55]
1.7 wt% PdO/Ce _{1-x} Pd _x O _{2-δ}	130	1.4	82	—	[56]
2.8 wt% Pd/SBA-15	110	0.2	7	73	[57]
1.2 wt% Pd/SrTiO ₃	100	0.2	19	91	[58]
1.6 wt% Pd/SSZ-13	120	0.2	13	60–80	[59]
6 wt% Pd/graphene	100	1.4	24	66	[60]
10 wt% Pd@SiO ₂	130	0.9	9	—	[61]
Pd-Zn/Al ₂ O ₃	135	—	66	72	[62]

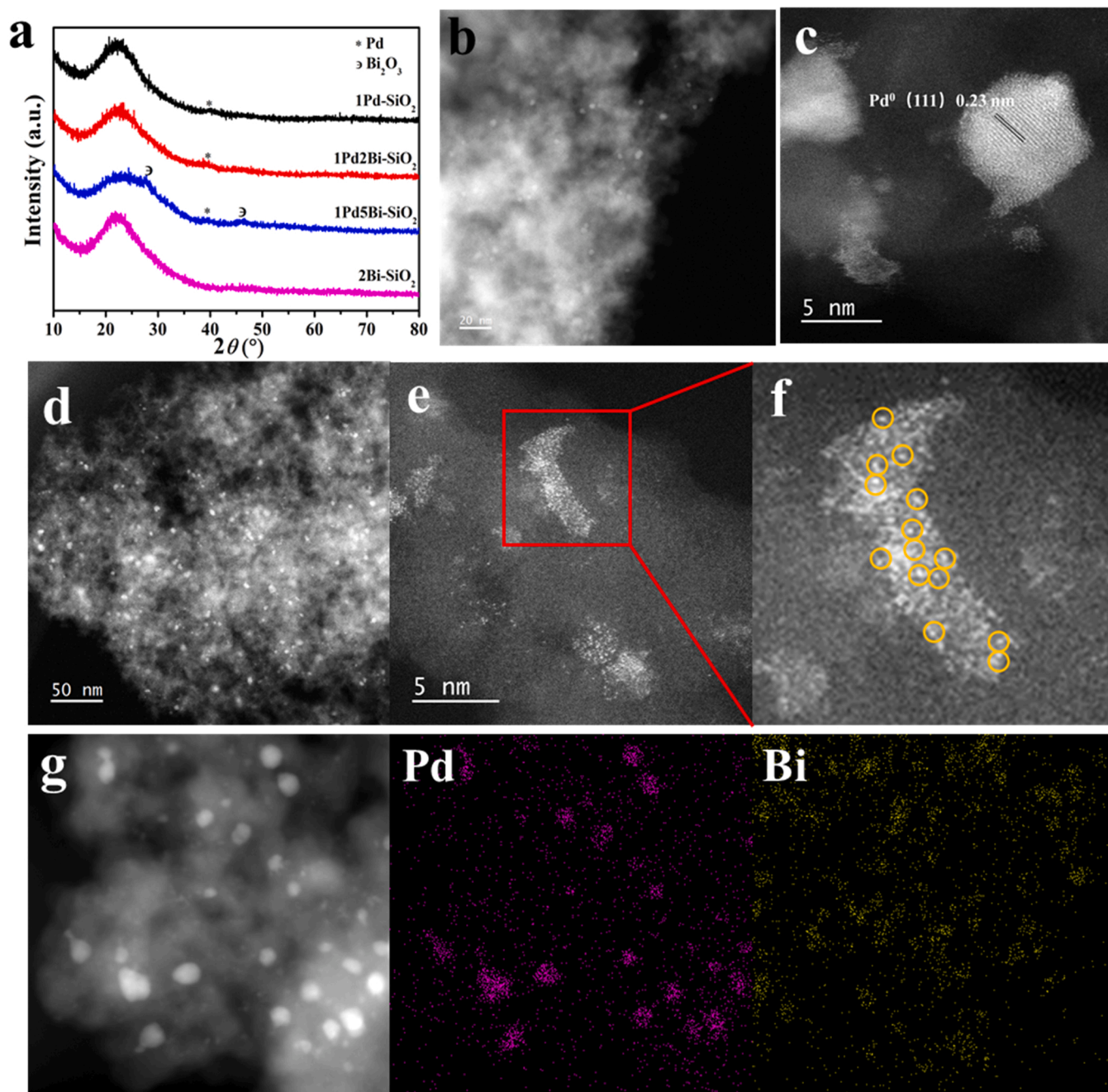


Fig. 4. (a) XRD profiles and (b-f) aberration-corrected HAADF-STEM images of used Pd/PdBi-SiO₂ samples: (b,c) 1 Pd-SiO₂ (d-f) 1Pd2Bi-SiO₂; (g) The corresponding aberration-corrected STEM-EDS elemental mapping images of used 1Pd2Bi-SiO₂ samples.

according to linear combination fitting results in Fig. S6. Meanwhile, on the basis of EXAFS fitting results (Fig. 5b and Table S2), strong metallic Pd-Pd ($R \approx 2.73$ Å, $CN \approx 7.0$) plus minor Pd-O ($R \approx 1.98$ Å, $CN \approx 1.4$) shells simultaneously were obtained in 1 Pd-SiO₂, indicating main phase was metallic Pd particles with partial palladium oxide species. The local coordination structure of palladium species in Bi-doped samples was also metallic Pd-Pd shell at 2.75 Å with a relatively low coordination number of 4.2–5.0, evidencing smaller palladium cluster size compared with that of 1 Pd-SiO₂. In addition, a Pd-O-Bi ($R \approx 3.36$ Å, $CN \approx 3.3$) shell was also detected only in 1Pd2Bi-SiO₂, which may be caused by oxidative atmosphere in reaction gas (1%CO/20%O₂/N₂). Because oxygen atoms in Pd_xBi_yO_z oxide clusters have been broken via hydrogen reduction before CO oxidation in Fig. S11. The in-situ CO-TPR results of used PdBi-SiO₂ sample also demonstrated that a few of surface oxygen

could be detected from Pd-O-Bi or PdO_x species in Fig. S12, which could promote CO oxidation activity.

Meanwhile, we have carried out XAFS experiments at Bi L₃ edge in Fig. 5c,d to clearly explore oxidation state and local coordination structure of Bi species in Bi-doped samples. Fig. 6c showed that bismuth species was mainly in Bi³⁺ state in used Bi-promoted catalysts with an average valence of + 2.8, due to excessive and isolated BiO_x clusters or single atoms on the surface of silica support. According to the H₂ -TPR profiles in Fig. 2e and 5e, this isolated bismuth species only was reduced with hydrogen reduction above 300 °C. Therefore, in EXAFS fitting results, there were strong Bi-O ($R \approx 2.14$ and $CN \approx 2.0$) plus Bi-O-Bi ($R \approx 3.89$ and $CN \approx 1.0$) [40] shells, originating from isolated BiO_x clusters in used PdBi-SiO₂ samples (Fig. 5d). More importantly, a metallic Bi-Pd shell ($R \approx 2.83$ Å, $CN \approx 0.5$) was determined for 1Pd2Bi-SiO₂ without

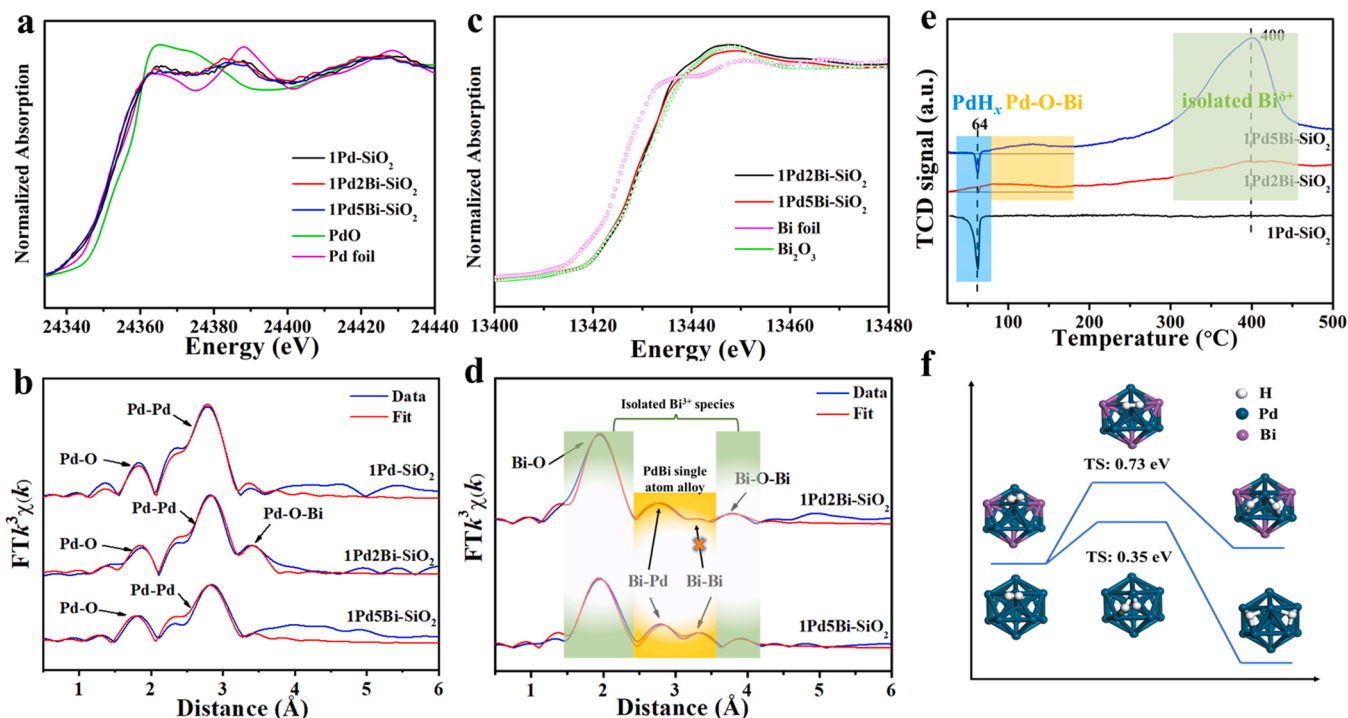


Fig. 5. *Ex-situ* XAFS measurements at Pd K-edge (a, b) and Bi L₃-edge (c, d): (a, c) XANES profiles and (b, d) EXAFS fitting results in R space of used Pd/PdBi-SiO₂ samples; (e) *In-situ* H₂ –TPR of used Pd/PdBi-SiO₂ samples after CO oxidation without air exposure; and (f) DFT results of H₂ dissociation on PdBi₁ single atom alloy.

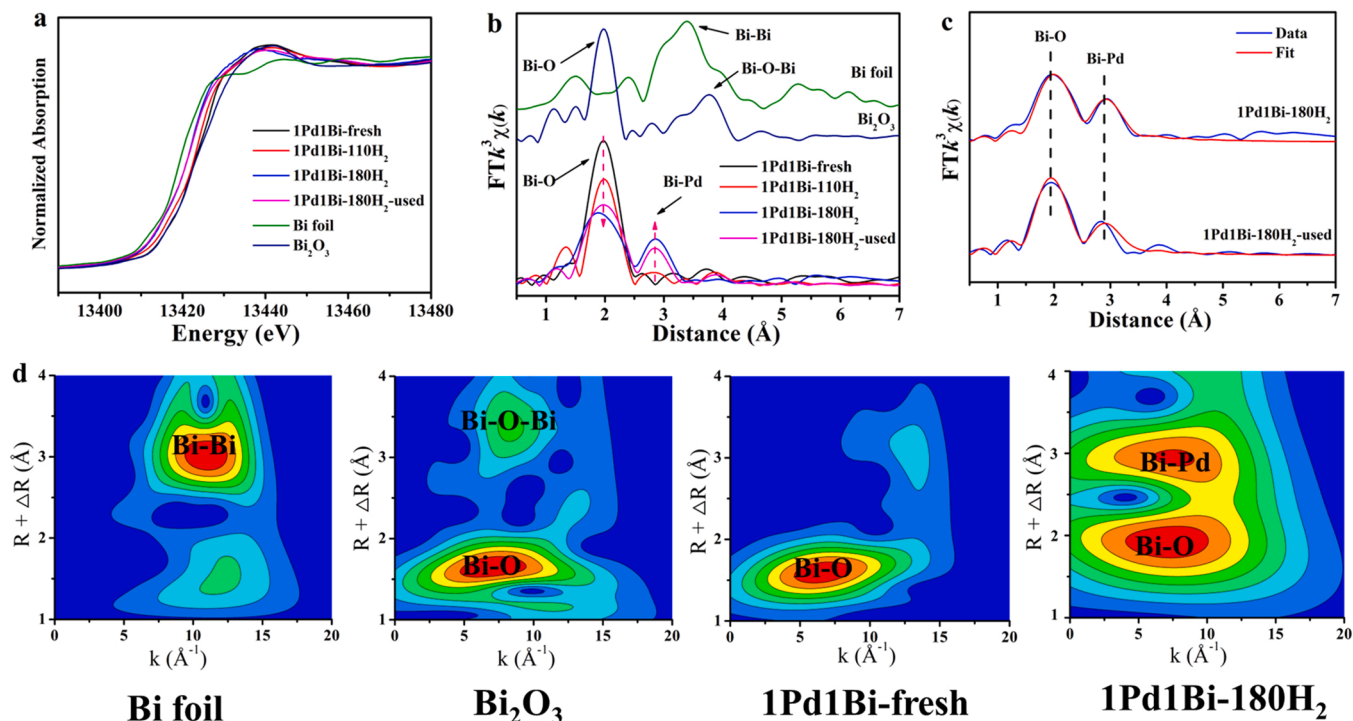


Fig. 6. *In-situ* XAFS measurements collected under different conditions on PdBi-SiO₂ catalysts. (a) Bi L₃-edge XANES spectra; (b,c) Bi L₃-edge EXAFS spectra and (d) the related WT plots for the Bi L₃-edge k³-weighted EXAFS signal for Bi foil, Bi₂O₃, 1Pd1Bi-fresh and 1Pd1Bi-180H₂.

any metallic Bi–Bi shell, which indicated that after hydrogen reduction bismuth was still at single atom level with no obvious aggregation. Combining the evidence of bright spots on palladium clusters in HAADF-STEM images in Fig. 4e,f, we can conclude that PdBi₁ single atom alloy with bismuth at atomic level formed after hydrogen reduction in 1Pd2Bi-SiO₂, which was the true active site. Previously, Shan

et al. reported the formation of PdNi alloy could lower apparent activation energy for CO oxidation to enhance catalytic activity [45]. According to the linear combination fitting results, about 7% of bismuth species were metallic state (Bi⁰) (Table S6). For 1Pd5Bi-SiO₂, an additional metallic Bi–Bi shell at 2.99 Å with a coordination number of ~0.6 was determined due to the aggregation of metallic bismuth, which was

the reason why 1 Pd5Bi-SiO₂ exhibited lower CO oxidation activity than 1 Pd2Bi-SiO₂.

In addition, we further found that PdBi₁ single atom alloy revealed absolutely different reducibility with metallic Pd particles from in-situ H₂ –TPR results after CO oxidation without air exposure (Fig. 5e). An obvious negative peak at 64 °C was observed for 1 Pd/SiO₂ in Fig. 5e caused by H₂ dissociation and desorption from metallic Pd nanoparticles below 100 °C[46]. However, the negative peak for Bi-promoted samples was much smaller than that of 1 Pd-SiO₂ under the condition of similar Pd oxidation state. Recently, Du et al. reported that PdBi alloy nanowire can restrain the expansion of PdH_x system[47]. Furthermore, the DFT calculation results also demonstrated that H₂ dissociation barrier energy on PdBi₁ single atom alloy (0.73 eV) was much higher than that (0.35 eV) of Pd cluster (Fig. 6f), which effectively suppress over-hydrogenation in some semi-hydrogenation reactions. Moreover, a broad reduction peak from 50 – 150 °C was observed in Bi-promoted catalysts, which originates from a small amount of Pd–O–Bi structure or Pd^{δ+} species (Fig. S13). The reduction peaks in of isolated BiO_x cluster or Bi^{δ+} single atom at ~400 °C in Bi-doped samples remained stable in Fig. 5e.

3.5. In-situ observation of formation for PdBi₁ single atom alloy via XAFS

In order to further uncover structure evolution of active site in PdBi-SiO₂ catalysts, in-situ XAFS experiments at Bi L₃ edge were collected in Fig. 6. According to ex-situ XAFS and H₂-TPR results, excessive and isolated bismuth species made a trouble in acquiring precise average oxidation state and structure evolution over Pd_xBi_yO_z cluster to PdBi₁ single atom alloy (Fig. S14 and S15). Therefore, we decided to decrease bismuth content to ~1 wt%, at the same time guaranteeing identical active structure with 1Pd2Bi-SiO₂ (Fig. 7). In Fig. 7a,b, in-situ XANES and EXAFS results indicated that bismuth species in fresh 1Pd1Bi-SiO₂ was total in Bi³⁺ state and only a strong Bi–O (*R* = 2.14 Å, CN = 2.3) was observed, demonstrating sole Bi³⁺ single atom. Furthermore, as the increase of hydrogen reduction temperature, the adsorption edge gradually shifted to lower energy, indicating the decrease of average oxide state over bismuth species, from 2.9 to 2.0. Accordingly, the intensity of Bi–O shell at ~2.14 Å and metallic Bi–Pd shell at ~2.82 Å progressively decreased and increased respectively. It indicated that Pd_xBi_yO_z binary oxide clusters was reduced to PdBi₁ single atom alloy without forming of any metallic Bi–Bi or Bi–O–Bi coordination bond,

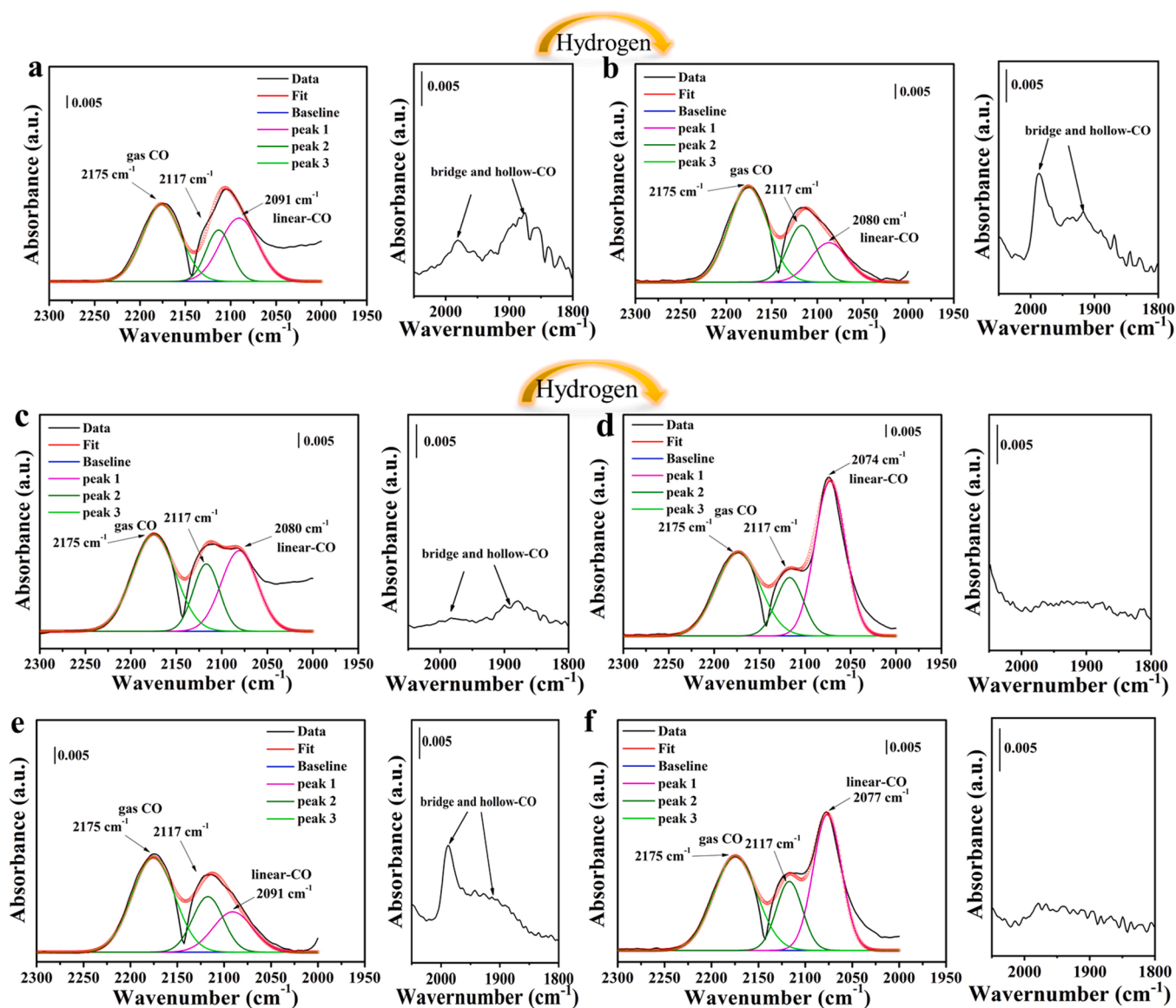


Fig. 7. CO adsorption on 1 Pd-SiO₂ (a,b,e) and 1Pd2Bi-SiO₂ (c,d,f) with different mode: (a,c) the samples was pretreated at 300 °C under air; (b,d) the samples was pretreated at 180 °C under H₂ flow; (e,f) after CO oxidation. (CO flow rate: 30 mL/min; catalyst mass: 20 mg; temperature: 120 °C).

evidencing bismuth species at single atom level (Fig. 7b and Table S7). In addition, the EXAFS spectra of 1Pd1Bi-SiO₂-180 H₂ and 1Pd1Bi-SiO₂-used exhibited almost identical coordination structure with Bi-Pd shell at ~ 2.82 Å and coordination number of ~ 1.0 , demonstrating that the active structure of PdBi₁ single atom alloy was stable during CO oxidation. Meanwhile, the DFT results in Fig. S16 also demonstrated that PdBi₁ single atom alloy exhibited better stability with higher cohesive energy, well consistent with CO oxidation stability test in Fig. 3e. Meanwhile, the wavelet transform (WT) of Bi L₃-edge EXAFS oscillations of standard sample and 1 Pd1Bi-SiO₂ was carried out, owing to its powerful resolutions in both K and R spaces (Fig. 7d). From the WT contour plots of 1Pd1Bi-SiO₂-180 H₂, Bi foil and Bi₂O₃, metallic Bi-Pd shell was absolutely different with metallic Bi-Bi and Bi-O-Bi shells.

3.6. The effect of restructuring on active site over adsorption behaviors in Pd/PdBi-SiO₂ catalysts

Based on in-situ XAFS and HAADF-STEM results, we have a clear understanding of active site structure: PdBi₁ single atom alloy with bismuth at atomic level in silica-supported palladium-bismuth catalysts. In addition, the adsorption behavior of reactant gas played a key role in catalytic activity. We further investigated CO adsorption on active site for Bi-free and Bi-doped catalysts. Fig. 8 and Fig. S17 have displayed CO adsorption of 1 Pd-SiO₂ and 1Pd2Bi-SiO₂ under different pretreatment conditions. Because of the overlap of gases CO and chemisorbed CO bands, the DRIFTS spectra were deconvoluted with Gaussian distribution based on realistic CO gas phase (fixed peaks position and area ratio, Fig. S17) and chemisorbed CO adsorption peak on Pd species under N₂

atmosphere (Fig. S18) to acquire reasonable CO adsorption results. The bands at 2117 and 2175 cm⁻¹ are attributed to gaseous CO [48]. As shown in Fig. S8a, both 1 Pd-SiO₂ and 1Pd2Bi-SiO₂ exhibited a poor catalytic activity for CO oxidation under oxidative pretreatment. The corresponding in-situ DRIFTS results with oxidative pretreatment in Fig. 7a,c showed a weak CO adsorption peak at 2091 and 2080 cm⁻¹ for Bi-free and Bi-doped samples respectively, which was attributed to linear adsorption of CO on metallic palladium (Pd⁰) species rather than palladium oxide phase [49]. It demonstrated a spontaneous variation in the extent of reduction of palladium sites occurs following the introduction of carbon monoxide. Meanwhile, the CO adsorption bands from 1800 to 2000 cm⁻¹ can be attributed to bridge- and hollow-CO adsorption approach because of the aggregation of Pd species [50]. The weak bridge- and hollow-CO peaks in 1 Pd2Bi-SiO₂ further validated higher dispersion of palladium sites compared with that of 1 Pd-SiO₂. Therefore, we can conclude that the poor adsorption ability of CO molecule is one reason of low activity for CO oxidation for both Bi-free and Bi-doped palladium-silica catalysts.

According to the catalytic performance in CO oxidation and structural characterization, the formation of PdBi₁ single atom alloy can significantly enhance CO oxidation activity for Bi-promoted samples. Thus, we carried out CO adsorption experiments with in-situ hydrogen reduction in DRIFTS cell before data collection. The CO frequency at 2080 cm⁻¹ was clearly seen in 1 Pd-SiO₂, which was assigned to CO molecule linearly adsorbing on metallic Pd species in Fig. 7b and the intensity of bridge- and hollow- CO bands between 1800 and 2000 cm⁻¹ became stronger than that of 1 Pd-SiO₂ with oxidative pretreatment (Fig. 7b and S19c). It indicated that the aggregation of palladium species

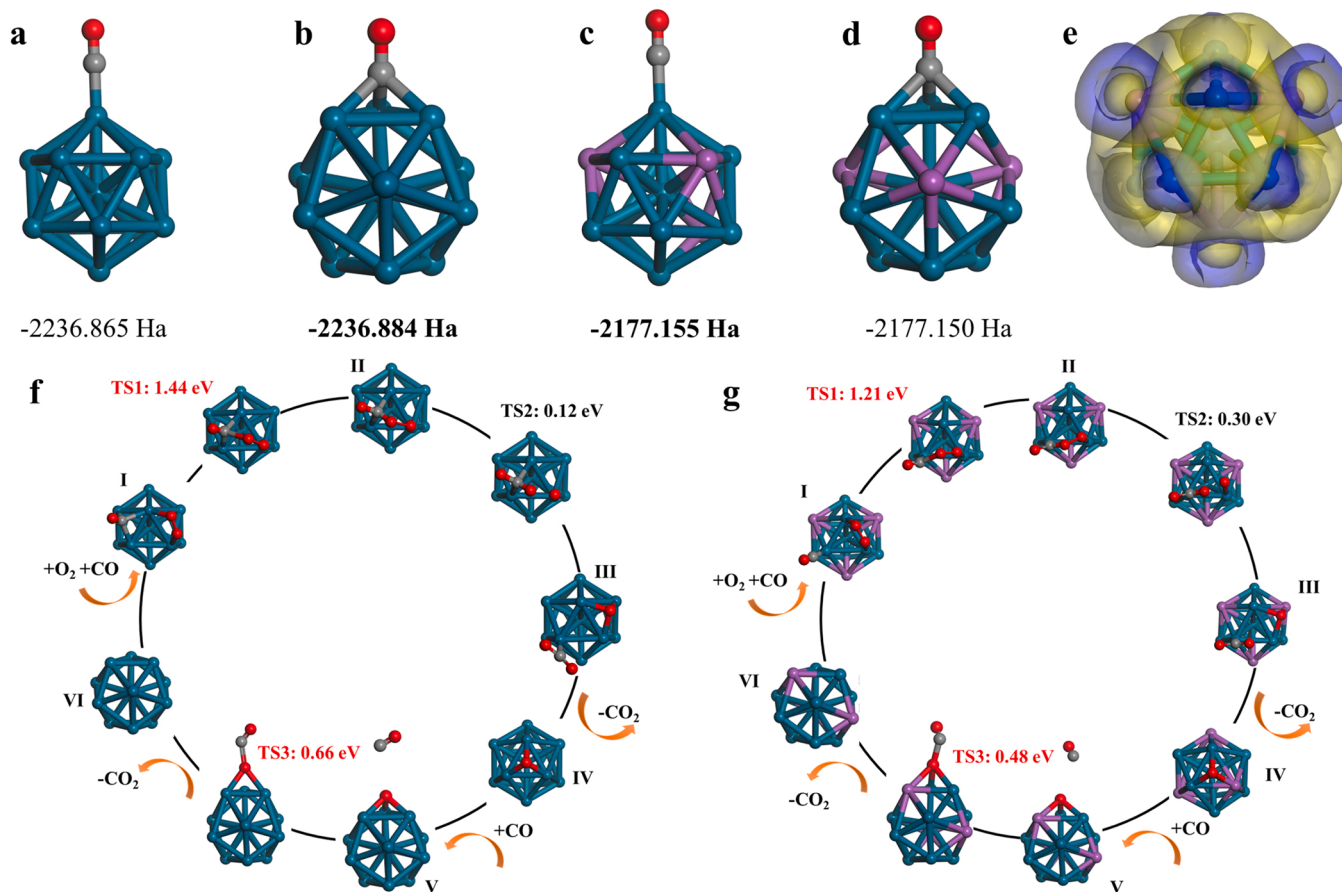


Fig. 8. DFT calculation results on metallic Pd nanoparticle and PdBi₁ single atom alloy. (a-d) different CO adsorption models on Pd particle (a,b) and PdBi₁ single atom alloy (c,d); (e) Mulliken charge analyses of PdBi₁ single atom alloy, blue and yellow represent losing and gaining electron respectively; (f,g) Proposed reaction mechanism for CO oxidation on Pd particle and PdBi₁ single atom alloy. Blue, purple, gray and red balls represent palladium, bismuth, carbon and oxygen atoms respectively.

occurs after the hydrogen reduction for pure Pd sample and the bridge- and hollow-CO adsorption methods are unfavorable for CO oxidation [51]. In comparison, only a CO frequency at 2074 cm^{-1} can be observed in reduced $1\text{Pd}2\text{Bi-SiO}_2$, which was attributed to linear adsorption of CO molecule on metallic Pd species with invisible bridge- and hollow-CO peaks in $1\text{Pd}2\text{Bi-SiO}_2$ (Fig. 7d). It demonstrated that CO only linearly adsorbed on PdBi_1 single atom alloy. The linear CO band at 2074 cm^{-1} for $1\text{Pd}2\text{Bi-SiO}_2$ can be eliminated the adsorption on isolated bismuth species in Fig. S17. Only gaseous CO peaks can be observed in pure bismuth sample (2Bi-SiO_2) under both oxidative and reduced pretreatment, revealing bismuth species possesses poor adsorption ability of CO molecule (Fig. S17). Furthermore, we found that the unique CO adsorption behavior on PdBi_1 single atom alloy was maintained for whole CO oxidation reaction in Fig. 7f. The linear CO bands at 2091 and 2077 cm^{-1} for 1Pd-SiO_2 and $1\text{Pd}2\text{Bi-SiO}_2$ respectively were similar to that after hydrogen reduction.

3.7. DFT calculations

In order to further investigate the intrinsic of adsorption behavior and reaction mechanism for pure Pd and PdBi_1 single atom alloy, we adopted icosahedron Pd_{13} and $\text{Pd}_{10}\text{Bi}_3$ cluster models, which were broadly used for metallic Pd^{52,53} and guarantee monoatomic dispersion of Bi for PdBi_1 single atom alloy respectively [54]. In Fig. 8a-d, the CO adsorption at different Pd site (top and hollow) were calculated, in which CO hollow- and top adsorption was energetically favorable for pure Pd and $\text{Pd}_{10}\text{Bi}_3$ single atom alloy respectively. On one hand, Mullikan charges results indicated that electrons were transferred from Bi to neighboring Pd atom about 0.1 |e| due to the difference of electronegativity, which also was proved by the deformation charges of Pd atom in $\text{Pd}_{10}\text{Bi}_3$ single atom alloy (Fig. 8e and S20). It was well consistent to the oxidation state of XANES results for Pd (+0.5) and PdBi_1 single atom alloy (+0.3). On the other hand, more electrons of Pd atom would fill up antibonding orbitals of CO, which went against CO further bonding with other palladium atom. Furthermore, the proposed reaction mechanisms for CO oxidation on pure Pd and PdBi_1 single atom alloy were shown in Fig. 8f,g. It was found that the barriers of the first step (LH mechanism) for forming CO-OO intermediates were 1.44 and 1.21 eV and the barriers of the second step (ER mechanism) for $\text{CO}+\text{O}\rightarrow\text{CO}_2$ were 0.66 and 0.48 eV for Pd particle and PdBi_1 single atom alloy respectively. It demonstrated that PdBi_1 single atom alloy exhibited lower barriers for CO and O_2 dissociation and better activity for CO oxidation, which was well consistent with our E_a value of $\sim 35\text{ kJ/mol}$ for $1\text{Pd}2\text{Bi-SiO}_2$. From the view of geometric effect, the unique structure (Pd_3 ensemble) in PdBi_1 single atom helped to shorten the distance between CO and O_2 molecules to form OO-CO intermediates and the neighboring Bi atom decreased O adsorption strength to accelerate CO oxidation. From the perspective of electron effect, Bi atoms transferring electrons to Pd_3 ensemble was conducive to strengthen OO-CO transition states and reduced the related formation barrier. We also plotted 4d states of Pd species in pure Pd and PdBi_1 single atom alloy (Fig. S21), in which 4d states entirely moved away from fermi level and reduced much more at fermi level. At the same time, smaller O adsorption energy (4.08 vs 4.64 eV) in PdBi_1 single atom alloy resulted in lower barrier for $\text{CO}+\text{O}\rightarrow\text{CO}_2$, which can lead to continuous and rapid CO oxidation. In addition, Pure Pd was easily covered by O atoms and oxidized to inactive Pd^{6+} species, resulting in less available active sites and higher E_a value ($\sim 50\text{ kJ/mol}$). Thus, the unique coordination and electron structure of PdBi_1 single atom alloy collectively resulted in the excellent CO oxidation activity.

4. Conclusions

In summary, we prepared a series of bismuth (Bi)-doped silica-supported Pd catalysts and found a hydrogen-controlled structural reconstruction mechanism of palladium-bismuth oxide cluster to single

atom alloy to efficiently catalyze low-temperature CO Oxidation. The formation of $\text{Pd}_3\text{Bi}_3\text{O}_x$ clusters with unique Pd–O–Bi coordination structure could enhance the sinter-resistance ability of Pd species. This structural evolution of active site is clearly uncovered by in-situ XAFS results, in which metallic Bi–Pd shell gradually generates as the increase of reduction temperature without any metallic Bi–Bi bond. More importantly, PdBi_1 single atom alloy exhibits a good CO oxidation activity with a CO_2 production rate of $413\text{ }\mu\text{mol}_{\text{CO}_2}\cdot\text{g}_{\text{Pd}}^{-1}\cdot\text{s}^{-1}$ at $100\text{ }^\circ\text{C}$ and excellent catalytic stability. DFT results indicate that there are geometric and electronic effects between Bi and Pd atoms, which favor total linear-CO adsorption, activate CO and O_2 molecules, and reduce the barrier for the formation of OO-CO intermediates in PdBi_1 single atom alloy.

CRedit authorship contribution statement

B.N. and L.L.L. developed platinum-bismuth catalysts, tested for catalytic activity, and prepared the article. L.L.G. and M.D. carried out the TEM/HRTEM images for all catalysts. Y.N.L. and X.T. measured in-situ DRIFTS data. Y.X.Z. made the DFT calculations. R.S. carried out XAS measurements and analyzed the data. C.M. carried out the aberration-correction HAADF-STEM and EDS mapping images of all catalysts. L.S. performed the CO-TPR experiments. B.N. and L.N.L. conceived and supervised the project, procured funds, and wrote the manuscript, with contributions from all authors.

Declaration of Competing Interest

The authors declare that they have no known competing financial interests or personal relationships that could have appeared to influence the work reported in this paper.

Data availability

Data will be made available on request.

Acknowledgments

This work was supported by “Photon Science Research Center for Carbon Dioxide”, Science and Technology Innovation Plan of Shanghai Science and Technology Commission (23YF1453700), “Shanghai Science and Technology Innovation Action Plan” (22JC1403800) and “2022 Self Deployed Instrument Design Project of Shanghai Advanced Research Institute”. We appreciate the assistance of TILON Group Technology Limited (Division of China), BL11B, the User Experiment Assist System and CAS-Shanghai Science Research Center of SSRF for data collection. We thank Dr. Shuang-quan Hu (Evonik Industries) for his kind help on supply of high surface-area silica support.

Appendix A. Supporting information

Supplementary data associated with this article can be found in the online version at [doi:10.1016/j.apcatb.2023.122818](https://doi.org/10.1016/j.apcatb.2023.122818).

References

- [1] J. Cha, et al., Highly monodisperse sub-nanometer and nanometer Ru particles confined in alkali-exchanged zeolite Y for ammonia decomposition, *Appl. Catal. B Environ.* 283 (2021), 119627.
- [2] F. Tao, et al., Reaction-driven restructuring of Rh-Pd and Pt-Pd core-shell nanoparticles, *Science* 322 (2008) 932–934.
- [3] J. Graciani, et al., Highly active copper-ceria and copper-ceria-titania catalysts for methanol synthesis from CO_2 , *Science* 345 (2014) 546–550.
- [4] Y.P. Zhai, et al., Alkali-stabilized Pt-OH_x species catalyze low-temperature water-gas shift reactions, *Science* 329 (2010) 1633–1636.
- [5] G.X. Pei, et al., Performance of Cu-alloyed Pd single-atom catalyst for semihydrogenation of acetylene under simulated front-end conditions, *ACS Catal.* 7 (2017) 1491–1500.
- [6] B. Nan, et al., Copper oxide clusters modified by bismuth single atoms to catalyze CO oxidation, *Appl. Catal. A Gen.* 636 (2022), 118578.

- [7] X. Wang, X.-P. Fu, W.-Z. Yu, C. Ma, C.-J. Jia, R. Si, Synthesis of a ceria-supported iron-ruthenium oxide catalyst and its structural transformation from subnanometer clusters to single atoms during the fischer–tropsch synthesis reaction, *Inorg. Chem. Front.* 4 (2017) 2059–2067.
- [8] F. Tao, et al., Evolution of structure and chemistry of bimetallic nanoparticle catalysts under reaction conditions, *J. Am. Chem. Soc.* 132 (2010) 8697–8703.
- [9] W.D. Michalak, et al., CO oxidation on PtSn nanoparticle catalysts occurs at the interface of Pt and Sn oxide domains formed under reaction conditions, *J. Catal.* 312 (2014) 17–25.
- [10] F. Tao, et al., Reaction-driven restructuring of Rh-Pd and Pt-Pd core-shell nanoparticles, *Science* 322 (2008) 932–934.
- [11] C.L. Hu, et al., Facet-evolution growth of $\text{Mn}_3\text{O}_4/\text{Co}_x\text{Mn}_{3-x}\text{O}_4$ electrocatalysts on Ni foam towards efficient oxygen evolution reaction, *J. Catal.* 369 (2019) 105–110.
- [12] W.Z. Yu, et al., Construction of active site in a sintered copper-ceria nanorod catalyst, *J. Am. Chem. Soc.* 141 (2019) 17548–17557.
- [13] T. Yang, et al., Enhanced fast response to Hg^0 by adsorption-induced electronic structure evolution of Ti_3C nanosheet, *Appl. Surf. Sci.* 544 (2021), 148925.
- [14] Z.-P. Wu, et al., Manipulating the local coordination and electronic structures for efficient electrocatalytic oxygen evolution, *Adv. Mater.* 33 (2021) 2103004.
- [15] M. Kim, et al., Controlling chemical turbulence by global delayed feedback: pattern formation in catalytic CO oxidation on Pt(110), *Science* 292 (2001) 1357–1360.
- [16] Y. Sun, et al., Ultrathin Co_3O_4 nanowires with high catalytic oxidation of CO, *Chem. Commun.* 47 (2011) 11279–11281.
- [17] G.J. Wu, N.J. Guan, L.D. Li, Low temperature CO oxidation on $\text{Cu}-\text{Cu}_2\text{O}/\text{TiO}_2$ catalyst prepared by photodeposition, *Catal. Sci. Technol.* 1 (2011) 601–608.
- [18] J. Ke, et al., Strong local coordination structure effects on subnanometer PtO_x clusters over CeO_2 nanowires probed by low-temperature CO oxidation, *ACS Catal.* 5 (2015) 5164–5173.
- [19] P.P. Du, et al., Synthesis and metal-support interaction of subnanometer copper-palladium bimetallic oxide clusters for catalytic oxidation of carbon monoxide, *Inorg. Chem. Front.* 4 (2017) 668–674.
- [20] T.-J. Huang, J.-F. Li, Direct methane oxidation over a Bi_2O_3 -GDC system, *J. Power Sources* 181 (2008) 62–68.
- [21] D.-D. Ma, D. Ding, J.-J. Huang, H. Zhang, Y.-P. Zheng, M.-S. Chen, H.-L. Wan, Promoting effect of bismuth oxide on palladium for low-temperature carbon monoxide oxidation, *ChemCatChem* 9 (2017) 499–504.
- [22] C. Mondelli, J.-D. Grunwaldt, D. Ferric, A. Baiker, Role of Bi promotion and solvent in platinum-catalyzed alcohol oxidation probed by in situ X-ray absorption and ATR-IR spectroscopy, *Phys. Chem. Chem. Phys.* 12 (2010) 5307–5316.
- [23] M.C. Figueiredo, et al., Direct alcohol fuel cells: increasing platinum performance by modification with sp-group metals, *J. Power Sources* 275 (2015) 341–350.
- [24] Q. Feng, et al., Isolated single-atom Pd sites in intermetallic nanostructures: high catalytic selectivity for semihydrogenation of alkynes, *J. Am. Chem. Soc.* 139 (2017) 7294–7301.
- [25] J.P. Simonovis, A. Hunt, R.M. Palomino, S.D. Senanayake, I. Waluyo, Enhanced stability of Pt-Cu single-atom alloy catalysts: in situ characterization of the Pt/Cu (111) surface in an ambient pressure of CO, *J. Phys. Chem. C* 122 (2018) 4488–4495.
- [26] M. Luneau, et al., Dilute Pd/Au alloy nanoparticles embedded in colloid-templated porous SiO_2 : stable Au-based oxidation catalysts, *Chem. Mater.* 31 (2019) 5759–5768.
- [27] G. Giannakakis, M. Flytzani-Stephanopoulos, E.C.H. Sykes, Single-atom alloys as a reductionist approach to the rational design of heterogeneous catalysts, *Acc. Chem. Res.* 52 (2019) 237–247.
- [28] H.C. Ham, et al., Importance of Pd monomer pairs in enhancing the oxygen reduction reaction activity of the $\text{AuPd}(1\ 0\ 0)$ surface: a first principles study, *Catal. Today* 263 (2016) 11–15.
- [29] J. Liu, et al., Tackling CO poisoning with single-atom alloy catalysts, *J. Am. Chem. Soc.* 138 (2016) 6396–6399.
- [30] H. Xie, et al., Boosting Pd-catalysis for electrochemical CO_2 reduction to CO on Bi-Pd single atom alloy nanodendrites, *Appl. Catal. B Environ.* 289 (2021), 119783.
- [31] H. Wang, et al., PdBi single-atom alloy aerogels for efficient ethanol oxidation, *Adv. Funct. Mater.* 31 (2021) 2103465.
- [32] B. Delley, From molecules to solids with the DMol3 approach, *J. Chem. Phys.* 113 (2000) 7756–7764.
- [33] B. Delley, Hardness conserving semilocal pseudopotentials, *Phys. Rev. B* 66 (2002), 155125.
- [34] M. Ernzerhof, G.E. Scuseria, Assessment of the perdue-burke-ernzerhof exchange-correlation functional, *J. Chem. Phys.* 110 (1999) 5029–5036.
- [35] J.P. Perdew, et al., Generalized gradient approximation made simple, *Phys. Rev. Lett.* 77 (1996) 3865–3868.
- [36] B. Nan, et al., Unique structure of active platinum-bismuth site for oxidation of carbon monoxide, *Nat. Comm.* 12 (2021) 3342.
- [37] J.-N. Park, et al., Highly active and sinter-resistant Pd-nanoparticle catalysts encapsulated in silica, *Small* 4 (2008) 1694–1697.
- [38] Y.-Y. Shen, Y. Sun, L.-N. Zhou, Y.-J. Li, E.S. Yeung, Synthesis of ultrathin PtPdBi nanowire and its enhanced catalytic activity towards p-nitrophenol reduction, *J. Mater. Chem. A* 2 (2014) 2977–2984.
- [39] Y. Mahara, K. Murata, K. Ueda, J. Ohyama, K. Kato, A. Satsuma, Time resolved in situ DXAFS revealing highly active species of PdO nanoparticle catalyst for CH_4 oxidation, *ChemCatChem* 10 (2018) 3384–3387.
- [40] M.A. Laguna-Marco, et al., Structural determination of Bi-doped magnetite multifunctional nanoparticles for contrast imaging, *Phys. Chem. Chem. Phys.* 16 (2014) 18301–18310.
- [41] Y.Y. Guo, C.N. Dai, Z.G. Lei, B.H. Chen, X.C. Fang, Synthesis of hydrogen peroxide over Pd/ SiO_2 /COR monolith catalysts by anthraquinone method, *Catal. Today* 276 (2016) 36–45.
- [42] A. Satsuma, K. Osaki, M. Yanagihara, J. Ohyama, K. Shimizu, Activity controlling factors for low-temperature oxidation of CO over supported Pd catalysts, *Appl. Catal. B Environ.* 132–133 (2013) 511–518.
- [43] Z. Hu, et al., Effect of ceria crystal plane on the physicochemical and catalytic properties of Pd/ceria for CO and propane oxidation, *ACS Catal.* 6 (2016) 2265–2279.
- [44] Y. Soni, S. Pradhan, M.K. Bamnia, A.K. Yadav, S.N. Jha, D. Bhattacharyya, T. S. Khan, M.A. Haider, C.P. Vinod, Spectroscopic evidences for the size dependent generation of pd species responsible for the low temperature CO oxidation activity on Pd-SBA-15 nanocatalyst, *Appl. Catal. B Environ.* 272 (2020), 118934.
- [45] S.Y. Shan, et al., Atomic-structural synergy for catalytic CO oxidation over palladium-nickel nanoalloys, *J. Am. Chem. Soc.* 136 (2014) 7140–7151.
- [46] A. López-Gaona, J.A. De los Reyes, Aguilar, J. Martín, N. Synthesis and characterization of Pt/MCM and Pd/MCM and its use in the hydrodechlorination of 1,2-dichloroethane, *Reac. Kinet. Mech. Cat.* 99 (2010) 177–182.
- [47] L.L. Du, et al., Palladium/bismuth nanowires with rough surface for stable hydrogen sensing at low temperatures, *ACS Appl. Nano Mater.* 2 (2019) 1178–1184.
- [48] K.L. Ding, et al., Identification of active sites in CO oxidation and water-gas shift over supported Pt catalysts, *Science* 350 (2015) 189–192.
- [49] H. Tiznado, S. Fuentes, F. Zaera, Infrared study of CO adsorbed on Pd/ Al_2O_3 -ZrO₂. effect of zirconia added by impregnation, *Langmuir* 20 (2004) 10490–10497.
- [50] H.D. Xu, et al., Entropy-stabilized single-atom Pd catalysts via high-entropy fluorite oxide supports, *Nat. Commun.* 11 (2020) 3908.
- [51] J. Xu, et al., Biphasic Pd-Au alloy catalyst for low-temperature CO oxidation, *J. Am. Chem. Soc.* 132 (2010) 10398–10406.
- [52] J. Meeprasert, et al., Capability of defective graphene-supported Pd₁₃ and Ag₁₃ particles for mercury adsorption, *Appl. Surf. Sci.* 364 (2016) 166–175.
- [53] X. Liu, L. Li, C. Meng, Y. Han, Palladium nanoparticles/defective graphene composites as oxygen reduction electrocatalysts: a first-principles study, *J. Phys. Chem. C* 116 (2012) 2710–2719.
- [54] Y. Zhang, J. Zhang, N. Zhang, L. Liu, A.A. Bokov, Z.-G. Ye, D. Wang, Hierarchical compositional ordering in lead-based perovskite relaxors, *Phys. Rev. B* 107 (2023), 054101.
- [55] J.R. Gaudet, A. Riva, E.J. Peterson, T. Bolin, A.K. Datye, Improved low-temperature CO oxidation performance of Pd supported on La-stabilized alumina, *ACS Catal.* 3 (2013) 846–855.
- [56] L. Meng, et al., Identification of active sites for CO and CH_4 oxidation over PdO/ $\text{Ce}_{1-x}\text{Pd}_x\text{O}_{2-8}$ catalysts, *Appl. Catal. B Environ.* 119–120 (2012) 117–122.
- [57] Y. Soni, et al., Spectroscopic evidences for the size dependent generation of Pd species responsible for the low temperature CO oxidation activity on Pd-SBA-15 nanocatalyst, *Appl. Catal. B Environ.* 272 (2020), 118934.
- [58] B.-R. Chen, et al., Morphology and CO oxidation activity of Pd nanoparticles on SrTiO_3 nanopolyhedra, *ACS Catal.* 8 (2018) 4751–4760.
- [59] A. Wang, et al., Insight into hydrothermal aging effect on Pd sites over Pd/LTA and Pd/SSZ-13 as PNA and CO oxidation monolith catalysts, *Appl. Catal. B Environ.* 278 (2020), 119315.
- [60] Y.Z. Li, et al., CO oxidation over graphene supported palladium catalyst, *Appl. Catal. B Environ.* 125 (2012) 189–196.
- [61] Y. Xu, et al., Palladium nanoparticles encapsulated in porous silica shells: an efficient and highly stable catalyst for CO oxidation, *RSC Adv.* 3 (2013) 851.
- [62] R.S. Johnson, et al., The CO oxidation mechanism and reactivity on PdZn alloys, *Phys. Chem. Chem. Phys.* 15 (2013) 7768.